The Astronomical Journal, 166:49 (14pp), 2023 August https://doi.org/10.3847/1538-3881/acdee8

A Mini-Neptune Orbiting the Metal-poor K Dwarf BD+29 2654

Fei Dai[1,2,42], Kevin C. Schlaufman[3], Henrique Reggiani[4], Luke Bouma[2,43], Andrew W. Howard[2], Ashley Chontos[5,6,41], Daria Pidhorodetska[7], Judah Van Zandt[8], Joseph M. Akana Murphy[9,44], Ryan A. Rubenzahl[2,44], Alex S. Polanski[10], Jack Lubin[11], Corey Beard[11], Steven Giacalone[12], Rae Holcomb[11], Natalie M. Batalha[13], Ian Crossfield[10], Courtney Dressing[14], Benjamin Fulton[15], Daniel Huber[6,16], Howard Isaacson[14,17], Stephen R. Kane[7], Erik A. Petigura[8], Paul Robertson[11], Lauren M. Weiss[18], Alexander A. Belinski[19], Andrew W. Boyle[20], Christopher J. Burke[21], Amadeo Castro-González[22], David R. Ciardi[23], Tansu Daylan[24,40], Akihiko Fukui[25,26], Holden Gill[12], Natalia M. Guerrero[21,27], Coel Hellier[28], Steve B. Howell[29], Jorge Lillo-Box[22], Felipe Murgas[30,31], Norio Narita[25,26,32], Enric Pallé[30], David R. Rodriguez[33], Arjun B. Savel[34], Avi Shporer[21], Keivan G. Stassun[35], Stephanie Striegel[29,36], Douglas A. Caldwell[29], Jon M. Jenkins[29], George R. Ricker[21], Sara Seager[21,37,38], Roland Vanderspek[21], and Joshua N. Winn[39]

[1] Division of Geological and Planetary Sciences, 1200 E California Boulevard, Pasadena, CA 91125, USA; fdai@caltech.edu
[2] Department of Astronomy, California Institute of Technology, Pasadena, CA 91125, USA
[3] William H. Miller III Department of Physics and Astronomy, Johns Hopkins University, 3400 N Charles Street, Baltimore, MD 21218, USA
[4] The Observatories of the Carnegie Institution for Science, 813 Santa Barbara Street, Pasadena, CA 91101, USA
[5] Department of Astrophysical Sciences, Princeton University, 4 Ivy Lane, Princeton, NJ 08540, USA
[6] Institute for Astronomy, University of Hawai'i, 2680 Woodlawn Drive, Honolulu, HI 96822, USA
[7] Department of Earth and Planetary Sciences, University of California, Riverside, CA 92521, USA
[8] Department of Physics & Astronomy, University of California Los Angeles, Los Angeles, CA 90095, USA
[9] Department of Astronomy and Astrophysics, University of California, Santa Cruz, CA 95064, USA
[10] Department of Physics and Astronomy, University of Kansas, Lawrence, KS 66045, USA
[11] Department of Physics & Astronomy, University of California Irvine, Irvine, CA 92697, USA
[12] Department of Astronomy, University of California Berkeley, Berkeley, CA 94720, USA
[13] Department of Astronomy and Astrophysics, University of California, Santa Cruz, CA 95060, USA
[14] 501 Campbell Hall, University of California at Berkeley, Berkeley, CA 94720, USA
[15] NASA Exoplanet Science Institute/Caltech-IPAC, MC 314-6, 1200 E California Boulevard, Pasadena, CA 91125, USA
[16] Sydney Institute for Astronomy, School of Physics, University of Sydney NSW 2006, Australia
[17] Centre for Astrophysics, University of Southern Queensland, Toowoomba, QLD 4350, Australia
[18] Department of Physics and Astronomy, University of Notre Dame, Notre Dame, IN 46556, USA
[19] Sternberg Astronomical Institute Lomonosov Moscow State University, Universitetskii prospekt, 119992, Moscow, Russia
[20] Department of Astronomy, California Institute of Technology, 1200 E. California Boulevard, Pasadena, CA 91125, USA
[21] Department of Physics and Kavli Institute for Astrophysics and Space Research, Massachusetts Institute of Technology, Cambridge, MA 02139, USA
[22] Centro de Astrobiología (CAB, CSIC-INTA), Depto. de Astrofísica, ESAC campus, E-28692, Villanueva de la Cañada (Madrid), Spain
[23] Caltech/IPAC-NASA Exoplanet Science Institute, 770 S. Wilson Avenue, Pasadena, CA 91106, USA
[24] Department of Astrophysical Sciences, Princeton University, Princeton, NJ 08544, USA
[25] Komaba Institute for Science, The University of Tokyo, 3-8-1 Komaba, Meguro, Tokyo 153-8902, Japan
[26] Instituto de Astrofísica de Canarias (IAC), E-38205 La Laguna, Tenerife, Spain
[27] Department of Astronomy, University of Florida, Gainesville, FL 32611, USA
[28] Astrophysics Group, Keele University, Staffordshire, ST5 5BG, UK
[29] NASA Ames Research Center, Moffett Field, CA 94035, USA
[30] Instituto de Astrofísica de Canarias (IAC), Calle Vía Láctea s/n, E-38205 La Laguna, Tenerife, Spain
[31] Departamento de Astrofísica, Universidad de La Laguna (ULL), E-38206 La Laguna, Tenerife, Spain
[32] Astrobiology Center, 2-21-1 Osawa, Mitaka, Tokyo 181-8588, Japan
[33] Space Telescope Science Institute, 3700 San Martin Drive, Baltimore, MD 21218, USA
[34] Department of Astronomy, University of Maryland, College Park, MD 20742, USA
[35] Department of Physics and Astronomy, Vanderbilt University, Nashville, TN 37235, USA
[36] SETI Institute, 339 N Bernardo Ave Suite 200, Mountain View, CA 94043, USA
[37] Department of Earth, Atmospheric and Planetary Sciences, Massachusetts Institute of Technology, Cambridge, MA 02139, USA
[38] Department of Aeronautics and Astronautics, MIT, 77 Massachusetts Avenue, Cambridge, MA 02139, USA
[39] Department of Astrophysical Sciences, Princeton University, 4 Ivy Lane, Princeton, NJ 08544, USA
Received 2023 April 28; revised 2023 June 6; accepted 2023 June 13; published 2023 July 7

Abstract

We report the discovery and Doppler mass measurement of a 7.4 days 2.3 $R_\oplus$ mini-Neptune around a metal-poor K dwarf BD+29 2654 (TOI-2018). Based on a high-resolution Keck/HIRES spectrum, the Gaia parallax, and

[40] LSSTC Catalyst Fellow.
[41] Henry Norris Russell Fellow.
[42] NASA Sagan Fellow.
[43] Pegasi b Fellow.
[44] NSF Graduate Research Fellow.

multiwavelength photometry from the UV to the mid-infrared, we found that the host star has $T_{\rm eff} = 4174^{+34}_{-42}$ K, $\log g = 4.62^{+0.02}_{-0.03}$, $[{\rm Fe/H}] = -0.58 \pm 0.18$, $M_* = 0.57 \pm 0.02\,M_\odot$, and $R_* = 0.62 \pm 0.01\,R_\odot$. Precise Doppler measurements with Keck/HIRES revealed a planetary mass of $M_{\rm p} = 9.2 \pm 2.1\,M_\oplus$ for TOI-2018 b. TOI-2018 b has a mass and radius that are consistent with an Earthlike core, with a ∼1%-by-mass hydrogen/helium envelope or an ice–rock mixture. The mass of TOI-2018 b is close to the threshold for runaway accretion and hence giant planet formation. Such a threshold is predicted to be around $10M_\oplus$ or lower for a low-metallicity (low-opacity) environment. If TOI-2018 b is a planetary core that failed to undergo runaway accretion, it may underline the reason why giant planets are rare around low-metallicity host stars (one possibility is their shorter disk lifetimes). With a *K*-band magnitude of 7.1, TOI-2018 b may be a suitable target for transmission spectroscopy with the James Webb Space Telescope. The system is also amenable to metastable Helium observation; the detection of a Helium exosphere would help distinguish between a H/He-enveloped planet and a water world.

Unified Astronomy Thesaurus concepts: Exoplanets (498); Mini Neptunes (1063); Ocean planets (1151)

Supporting material: machine-readable table

1. Introduction

The occurrence rate of giant planets is strongly correlated with the host star metallicity (Gonzalez 1997; Santos et al. 2004; Fischer & Valenti 2005). This strong correlation has been regarded as supporting evidence for the core accretion theory of planet formation (Pollack et al. 1996). In a metal-rich disk, a high abundance of solid materials helps planet embryos grow quickly to the critical mass that initiates runaway gas accretion and gas-giant formation. On the other hand, the close-in, sub-Neptune planets (<1 au, 1–4$R_\oplus$, also known as the Kepler-like planets) are much more common around solar-type stars compared to giant planets (e.g., Howard et al. 2012; Fressin et al. 2013; Petigura et al. 2013). The occurrence rate of sub-Neptune planets also has a much weaker dependence on host metallicity compared to the giant planets (e.g., Wang & Fischer 2015; Petigura et al. 2018). One might argue that the formation of gas-giant planets may be a threshold-crossing event that has to occur when the gaseous disk is still present. On the other hand, the formation of sub-Neptune planets is less demanding on the core assembly rate and can proceed in low-metallicity environments. The super-Earth planets may not accrete a substantial envelope (Rogers 2015), whereas the mini-Neptunes only acquire their envelopes toward the final vestige of the disk, when the disk starts to become optically thin (Lee & Chiang 2016; Lee et al. 2018).

So far, most planet occurrence studies (e.g., Kepler Borucki et al. 2011) have been based on surveys of stars with Sunlike metallicities [Fe/H] between −0.5 and 0.5. It is not clear how the occurrence–metallicity correlation extends to a more metal-depleted regime ([Fe/H] <−0.5). The standard minimum-mass solar nebula (Hayashi 1981) has about $30M_\oplus$ of solid materials within the innermost 1 au for the in situ formation of the close-in sub-Neptune planets. The total amount of solid materials would decrease to 3–9 $M_\oplus$ for $-1 < [{\rm Fe/H}] < -0.5$. Such a limited supply of solids may prevent the formation of multiple close-in sub-Neptune planets.

To further investigate the influence of host metallicity, we (K. Schlaufman et al. 2023, in preparation) are studying the occurrence rate of transiting sub-Neptune planets around metal-poor ($-1 < [{\rm Fe/H}] < -0.5$) stars observed as the TESS mission (Ricker et al. 2014). Thanks to the nearly full-sky coverage of TESS, we were able to crossmatch the TESS Input Catalog (Stassun et al. 2019) with ground-based spectroscopic surveys, including the Large Sky Area Multi-Object Fiber Spectroscopic Telescope Low-Resolution Survey Data Release (DR) 6 (Cui et al. 2012), the Radial Velocity Experiment DR6 (Steinmetz et al. 2020), and the GALactic Archaeology with Hermes (GALAH) DR3 (Buder et al. 2021). We identified a sample of about 10,000 dwarf stars with $-1 < [{\rm Fe/H}] < -0.5$. We have carried out a systematic search for transiting planets among this sample. This search led to the discovery of BD+29 2654, which was also discovered independently by the TESS team as TOI-2018 (Guerrero et al. 2021). TOI-2018 is a bright, nearby K dwarf among our transiting planet hosts that is particularly amenable to follow-up observations. We also present an additional transiting signal, TOI-2018.02, which was not reported by the TESS team (Guerrero et al. 2021) due to its lower signal-to-noise ratio (S/N). We carried out a detailed characterization of the host star and Doppler mass measurements of the planets to help the community plan follow-up observations of this system.

The paper is organized as follows. Section 2 presents a detailed characterization of the host star TOI-2018, with particular attention to its metallicity. Section 3 describes our transit detection and modeling of this system based on the light curves. In Section 4, we present the radial velocity (RV) measurements of TOI-2018 and the resultant constraints on the planetary masses. Section 5 discusses the implications of our findings.

2. Stellar Properties

2.1. Fundamental and Photospheric Parameters

To derive the stellar parameters, we analyzed an archival high-resolution, high-S/N spectrum of TOI-2018 taken with the High Resolution Echelle Spectrometer on the 10 m Keck Telescope (Keck/HIRES; Vogt et al. 1994) on 2012 July 26. The spectrum was taken without the iodine cell and it reached an S/N of about 200 per reduced pixel near 5500 Å after a 600 s exposure. We made use of both spectroscopy and isochrones to infer the photospheric and fundamental stellar parameters, as described in Reggiani et al. (2022). Isochrones are especially useful for determining the effective temperature $T_{\rm eff}$ of the star, because high-quality multiwavelength photometry from the UV to the red optical is available. Similarly, the availability of the Gaia DR3 parallax-based distance of TOI-2018 makes the calculation of surface gravity $\log g$ via isochrones more straightforward than it has traditionally been. With good constraints on both $T_{\rm eff}$ and $\log g$ from isochrone fitting, the equivalent widths (EWs) of iron lines can be used to determine metallicity [Fe/H] and microturbulence ξ by minimizing the dependence of individual line-based iron abundance inferences on their reduced EWs.

The inputs to our photospheric and fundamental stellar parameter inference are the EWs of Fe I and Fe II atomic absorption lines, multiwavelength photometry, the Gaia parallax,

and an extinction estimate. Using atomic absorption line data from Yana Galarza et al. (2019) for lines that are relatively insensitive to stellar activity (Meléndez et al. 2014), we measured the EWs by fitting Gaussian profiles with the `splot` task in `IRAF` to our continuum-normalized spectrum. We also confirmed our `splot` EWs by remeasuring the lines using `iSpec` (Blanco-Cuaresma et al. 2014; Blanco-Cuaresma 2019). We only compared the clean (unblended) lines with our `splot` measurements and we concluded that there were no substantial differences in the EWs measured with `splot` and `iSpec`. For the blended lines, we used the `deblend` task to disentangle absorption lines from adjacent spectral features. We gathered *u* photometry and their uncertainties from Sloan Digital Sky Survey (SDSS) DR13 (Albareti et al. 2017), *G* photometry and its uncertainty from Gaia DR2 (Gaia Collaboration et al. 2016, 2018; Arenou et al. 2018; Evans et al. 2018; Hambly et al. 2018; Riello et al. 2018), *J*, *H*, and *Ks* from the Two Micron All Sky Survey (2MASS), and *W*1 and *W*2 from the Wide-field Infrared Survey Explorer (WISE). We use the Gaia DR3 parallax and its uncertainty (Fabricius et al. 2021; Lindegren et al. 2021a, 2021b; Torra et al. 2021; Gaia Collaboration et al. 2023), as well as an extinction A_V inference based on three-dimensional (3D) maps of extinction in the solar neighborhood from the STructuring by Inversion the Local Interstellar Medium program (Lallement et al. 2014, 2018; Capitanio et al. 2017). We assume Asplund et al. (2021) solar abundances. To derive the stellar parameters, we use the `isochrones` package by Morton (2015) to fit the MESA Isochrones and Stellar Tracks (MIST; e.g., Paxton et al. 2011, 2013, 2015; Choi et al. 2016) to the photospheric parameters as well as the multiwavelength photometry, parallax, and extinction using the nested sampling code `MultiNest` (Feroz et al. 2009, 2013). We present the stellar parameters in Table 1. We would like to remind readers that the stellar parameters derived from isochrone models are often subject to substantial systematic uncertainties between different isochrone models (e.g., 4% in stellar radius; Tayar et al. 2022). These are not explicitly included in the reported values here. As an additional check, we inferred $T_{\rm eff}$ of TOI-2018 using the `colte` code[45] (Casagrande et al. 2021), which estimates $T_{\rm eff}$ using a combination of color–$T_{\rm eff}$ relations obtained by implementing the InfraRed Flux Method for Gaia and 2MASS photometry. As required by `colte`, we used Gaia DR3 *G*, $G_{\rm BP}$, and $G_{\rm RP}$ plus 2MASS *J*, *H*, and K_s photometry as input. We find a `colte`-based $T_{\rm eff} = 4160 \pm 81$ K, consistent with our isochrone-inferred effective temperature. We could not measure the rotational broadening *v*sin*i* of the host star, given the resolution of our HIRES spectrum. The *v*sin*i* is likely smaller than 2 km s^{-1} (this is consistent with the 23.5 days rotation period we determine in Section 3).

2.2. Chemical Abundances

To infer the elemental abundances, we first measured the EWs of the atomic absorption lines of Na I, Mg I, Al I, Si I, K I, Ca I, Sc II, Ti I, Ti II, V I, Cr I, Fe I, Fe II, Ni I, Co I, Y II, and Ba II in our continuum-normalized spectrum by fitting Gaussian profiles with `iSpec`. We avoid blended lines and only kept lines with EWs smaller than 170 mÅ. We assume Asplund et al. (2021) solar abundances and local thermodynamic equilibrium (LTE) and we used the 1D plane-parallel solar composition MARCS model atmospheres (Gustafsson et al. 2008) and the 2019 version of `MOOG` (Sneden 1973; Sneden et al. 2012) to infer elemental abundances based on each EW measurement. We report our adopted atomic data, EW measurements, and individual line-based abundance inferences in Table 2. We report our abundance inferences in three common systems: *A*(X), [X/H], and [X/Fe]. The abundance *A*(X) is defined as $A(\mathrm{X}) = \log N_{\rm X}/N_{\rm H} + 12$, the abundance ratio [X/H] is defined as $[\mathrm{X/H}] = A(\mathrm{X}) - A(\mathrm{X})_\odot$, and the abundance ratio [X/Fe] is defined as $[\mathrm{X/Fe}] = [\mathrm{X/H}] - [\mathrm{Fe/H}]$. We define the uncertainty in the abundance ratio $\sigma_{[\mathrm{X/H}]}$ as the standard deviation of the individual line-based abundance inferences $\sigma_{[\mathrm{X/H}]}{}'$ divided by $\sqrt{n_{\rm X}}$, where n is the number of lines used. We define the uncertainty $\sigma_{[\mathrm{X/Fe}]}$ as the square root of the sum of the squares of $\sigma_{[\mathrm{X/H}]}$ and $\sigma_{[\mathrm{Fe/H}]}$. The results are reported in Table 3.

Table 1
Adopted Stellar Parameters

Property	Value	Unit
SDSS DR13 *u*	13.385 ± 0.0264	AB mag
Gaia DR2 *G*	9.720 ± 0.002	Vega mag
2MASS *J*	7.844 ± 0.021	Vega mag
2MASS *H*	7.255 ± 0.020	Vega mag
2MASS *K*	7.104 ± 0.017	Vega mag
WISE W1	6.984 ± 0.062	Vega mag
WISE W2	7.071 ± 0.020	Vega mag
Gaia DR3 parallax	35.666 ± 0.014	mas
Spectroscopically Inferred Parameters		
[Fe/H]	-0.58 ± 0.18	
*v*sin*i*	<2	km s^{-1}
S_{HK}	0.92 ± 0.03	
$\log R'_{\rm HK}$	-4.75 ± 0.04	
Isochrone-inferred Parameters		
Effective temperature $T_{\rm eff}$	4174^{+34}_{-42}	K
Surface gravity $\log g$	$4.62^{+0.02}_{-0.03}$	cm s^{-2}
Stellar mass M_*	0.57 ± 0.02	$M_\odot$
Stellar radius R_*	0.62 ± 0.01	$R_\odot$
Luminosity L_*	0.10 ± 0.01	$L_\odot$
Distance	28.038 ± 0.011	pc

Note. Substantial systematic uncertainties may exist between different isochronal models (Tayar et al. 2022).

2.3. Age, Spectral Energy Distribution, and Thick-disk membership

To check on the system age, we measured a stellar rotation period of 23.5 ± 1.0 days in the WASP light curve of TOI-2018 using the Lomb–Scargle periodogram (Lomb 1976; Scargle 1982); the autocorrelation function (McQuillan et al. 2014) gives a consistent result. The rotation period translates to a gyrochronological age of 1.6 ± 0.1 Gyr according to the scaling relation of Mamajek & Hillenbrand (2008). If we use the more up-to-date empirical relations of Bouma et al. (2023), TOI-2018's rotation period indicates an age of 2.4 ± 0.2 Gyr. We also analyzed the chromospheric activity as seen in the Ca II H and K lines of our HIRES spectrum. We found the activity indicator $S_{HK} = 0.92 \pm 0.03$ and $\log R'_{\rm HK} = -4.75 \pm 0.04$ using the method of Isaacson & Fischer (2010). The activity level of TOI-2018 is at about the fiftieth percentile (see Figure 1) of stars with similar *B*–*V* color (within 0.1 in *B*–*V*) as observed by the California Planet Search

[45] https://github.com/casaluca/colte

Table 2
Atomic Data, EWs, and Line Abundances

Wavelength (Å)	Species	Excitation Potential (eV)	log(*gf*)	EW (mÅ)	$\log_{\epsilon}$(X)
4751.822	NaI I	2.104	−2.078	41.30	5.824
6154.225	NaI I	2.102	−1.547	82.90	5.721
6160.747	NaI I	2.104	−1.246	95.30	5.528
4730.029	MgI I	4.346	−2.347	110.30	7.475
5711.088	MgI I	4.346	−1.724	116.30	7.004
6318.717	MgI I	5.108	−2.103	37.60	7.498
4512.268	CaI I	2.526	−1.900	63.50	5.617
5260.387	CaI I	2.521	−1.719	71.70	5.650
5512.980	CaI I	2.933	−0.464	167.10	5.462
5867.562	CaI I	2.933	−1.570	64.40	5.771
6166.439	CaI I	2.521	−1.142	126.30	5.352

Note. Full version online. This table is published in its entirety in machine-readable format. A portion is shown here for guidance regarding its form and content.

(This table is available in its entirety in machine-readable form.)

Table 3
Elemental Abundances

Species	*A*(X)	[X/H]	$\sigma_{[X/H]}$	[X/Fe]	$\sigma_{[X/Fe]}$	*n*
LTE Abundances						
Na I	5.691	−0.529	0.123	0.051	0.089	3
Mg I	7.326	−0.224	0.228	0.356	0.169	3
Al I	5.796	−0.634	0.031	−0.054	0.032	2
Si I	7.230	−0.280	0.246	0.300	0.260	2
Ca I	5.570	−0.730	0.147	−0.150	0.077	5
Sc I	2.622	−0.518	0.207	0.062	0.151	3
Ti II	4.624	−0.346	0.194	0.234	0.099	7
V I	3.543	−0.357	0.281	0.223	0.120	7
Cr II	4.951	−0.669	0.000	−0.089	0.120	1
Fe I	6.880	−0.580	0.171	⋯	⋯	70
Fe II	6.963	−0.497	0.082	⋯	⋯	4
Co I	4.724	−0.216	0.185	0.364	0.087	6
Ni I	5.947	−0.253	0.307	0.327	t 0.105	13
Cu I	4.035	−0.144	0.062	0.436	0.059	4
Y II	1.260	−0.950	0.000	−0.370	0.033	1
Ba II	1.519	−0.751	0.001	−0.171	0.025	2

(Howard et al. 2010). In addition, we looked for Lithium absorption in our HIRES spectrum of TOI-2018. We could not detect a Lithium feature that is statistically significant above the nearby continuum. We note that both the strength of Lithium absorption and $\log R'_{\rm HK}$ are likely correlated with the host star metallicity [Fe/H]. The existing samples are dominated by solar metallicity stars. If TOI-2018 is indeed a thick-disk star, as we will discuss shortly, one might expect it to be old (>8–9 Gyr). A previous work by Martig et al. (2015), however, reported a curious sample of young, α-enhanced stars in the solar neighborhood. Given the quality and discrepancy of the various age indicators, we are unable to provide a precise age constraint on TOI-2018, as is often the case for late-type stars.

We further examined the kinematics of TOI-2018. The proper motion of TOI-2018 does not fit any known comoving associations reported in `Banyan-Σ` (Gagné et al. 2018) and in Bouma et al. (2022). We also computed the Galactic UVW velocity of TOI-2018 (U,V,W = −59.6, 11.4, −8.9 km s^{-1}). Using the framework of Bensby et al. (2014), TOI-2018 has a 3.1% chance of being in the thick disk based on its kinematics alone.

We also investigated the α-element enhancement of TOI-2018. Using Mg, Si, and Ti abundances as a proxy for the α elements (we excluded Ca due to its association with stellar activity), we obtained $[\alpha/\mathrm{Fe}] = 0.29 \pm 0.12$. In Figure 2, we plot $[\alpha/\mathrm{Fe}]$ against [Fe/H] for TOI-2018 and a crossmatch between the GALAH survey (e.g., Buder et al. 2021) and the TESS Input Catalog (Stassun et al. 2019) as presented in Carrillo et al. (2020). The α-element enhancement of TOI-2018 does favor a thick-disk membership. However, this claim needs to be further confirmed with more precise $[\alpha/\mathrm{Fe}]$ and kinematic constraints.

We fitted the spectral energy distribution (SED) of TOI-2018 following the method of Stassun & Torres (2016). We fitted Kurucz stellar atmosphere models (Kurucz 1979) to various photometric bands. Our fit yielded a reduced χ^2 of 1.1. We obtained a stellar mass and radius of $0.59 \pm 0.04 M_{\odot}$ and $0.62 \pm 0.02 R_{\odot}$, which are consistent with our isochronal analysis. We did not find any evidence for an infrared excess that may be attributable to a debris disk (Figure 3).

2.4. High-resolution Imaging

As part of our standard process for validating transiting exoplanets, and to assess the contamination of bound or unbound companions on the derived planetary radii (Ciardi et al. 2015), we observed TOI-2018 with high-resolution imaging. The star was observed with Palomar/PHARO (Hayward et al. 2001), Lick/ShARCS (Kupke et al. 2012; Gavel et al. 2014; McGurk et al. 2014), Gemini-N/Alopeke (Howell et al. 2011), Caucasian Observatory of Sternberg Astronomical Institute/Speckle Polarimeter (Safonov et al. 2017), and Carlo Alto/AstraLux (Hormuth et al. 2008), thanks to the efforts of the TESS Follow-up Observing Program Working Group.

We present the Palomar/PHARO result here as an example. All other high-resolution imaging results did not detect any nearby stellar companions, and they are available on the ExoFOP website.[46] The Palomar observations were made with the PHARO instrument (Hayward et al. 2001) behind the natural guide star adaptive optics (AO) system P3K (Dekany et al. 2013) on 2021 June 19 UT in a standard five-point quincunx dither pattern with steps of 5″ in the narrowband $Br-\gamma$ filter ($\lambda_o = 2.1686$; $\Delta\lambda = 0.0326$ μm). Each dither position was observed three times, offset in position from each other by 0.″5, for a total of 15 frames; with an integration time of 1.4 s per frame, the total on-source time was 14 s. PHARO has a pixel scale of 0.″025 per pixel for a total field of view of ∼25″. The science frames were flat-fielded and sky-subtracted. The reduced science frames were combined into a single combined image with a final resolution of 0.″091 FWHM.

To within the limits of the AO observations, no stellar companions were detected. The sensitivities of the final combined AO image were determined by injecting simulated sources azimuthally around the primary target every 20° at separations of integer multiples of the central source's FWHM (Furlan et al. 2017; Lund & Ciardi 2020). The brightness of each injected source was scaled until standard aperture photometry detected it with 5σ significance. The resulting

[46] https://exofop.ipac.caltech.edu/tess/

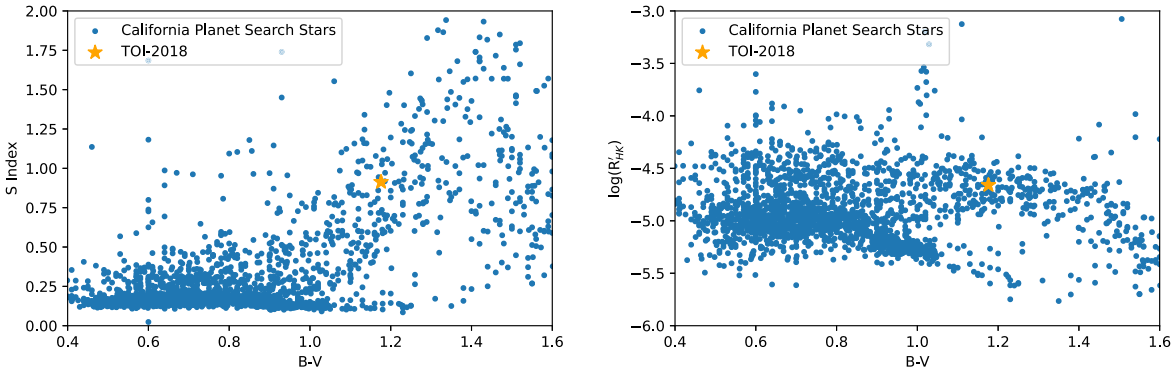

Figure 1. The chromospheric activity of TOI-2018 (orange star) in comparison with other stars in the California Planet Search sample (Isaacson & Fischer 2010). Both S_{HK} and $\log R'_{\rm HK}$ are close to the fiftieth percentile of stars with similar B–V color. Unfortunately, the star is too cool to apply previously calibrated age–activity relations (e.g., Mamajek & Hillenbrand 2008).

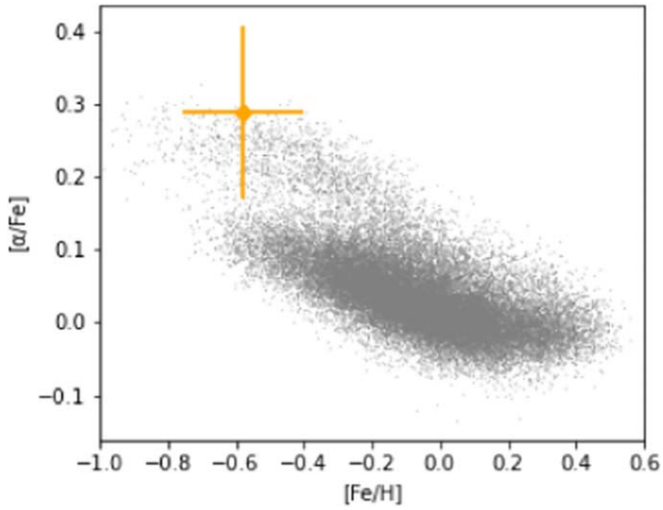

Figure 2. TOI-2018 is α-element enhanced and [α/Fe]-depleted, which is suggestive of a thick-disk star. However, the kinematics (UVW) of TOI-2018 only gives a 3.1% chance of being a thick-disk star. The thick-disk membership of the system needs further confirmation. The gray points are [α/Fe] and [Fe/H] for the TESS Input Catalog (Stassun et al. 2019) as presented in Carrillo et al. (2020).

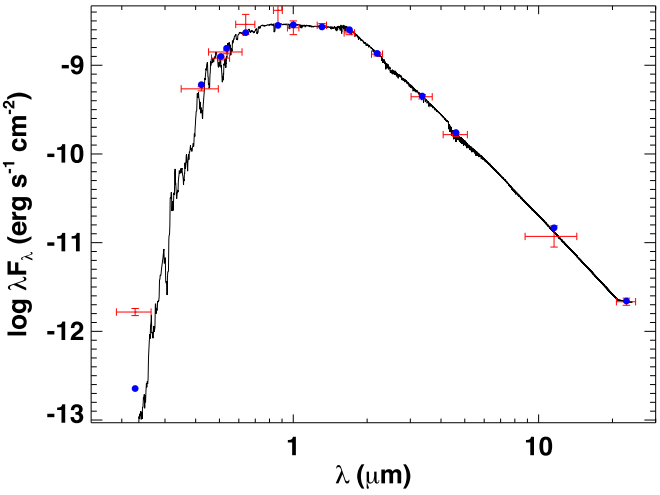

Figure 3. The SED of TOI-2018. The red symbols are the various reported photometric measurements of the system (see the text). The horizontal error bars indicate the effective widths of the passbands. The black curve is the best-fit Kurucz atmosphere model (Kurucz 1979), while the blue symbols are the integrated model flux within each passband. No obvious infrared excess is detected.

brightness of the injected sources relative to TOI-2018 set the contrast limits at that injection location. The final 5σ limit at each separation was determined from the average of all of the determined limits at that separation. The uncertainty on the limit was set by the rms dispersion of the azimuthal slices at a given radial distance (Figure 4).

In addition to the high-resolution imaging, we also utilized Gaia to identify any wide stellar companions that may be bound members of the system. Typically, these stars are already in the TESS Input Catalog and their flux dilution to the transit has already been accounted for in the transit fits and associated derived parameters. Based upon similar parallaxes and proper motions (e.g., Mugrauer & Michel 2020, 2021; Mugrauer et al. 2022), there are no additional widely separated companions identified by Gaia. Additionally, the Gaia DR3 astrometry provides additional information on the possibility of inner companions that may have gone undetected by either Gaia or high-resolution imaging. The Gaia Renormalized Unit Weight Error (RUWE) is a metric similar to a reduced chi-square, where values that are $\lesssim$1.4 indicate that the Gaia astrometric solution is consistent with the star being single. In contrast, RUWE values $\gtrsim$1.4 may indicate an astrometric

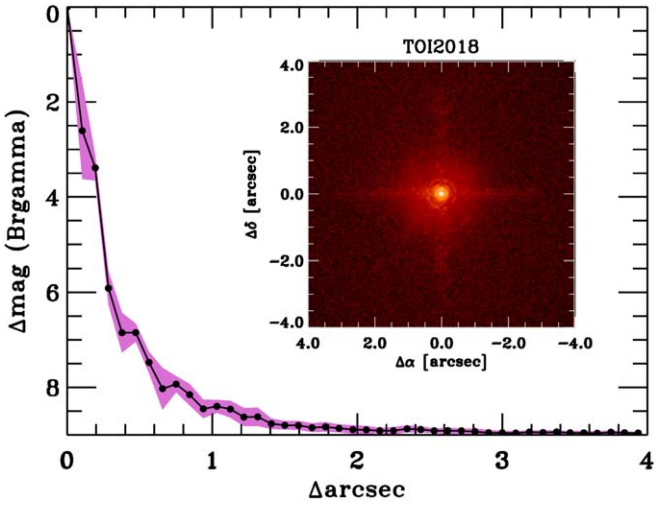

Figure 4. Companion sensitivity for the near-infrared AO imaging. The black points represent the 5σ limits and are separated in steps of 1 FWHM; the purple represents the azimuthal dispersion (1σ) of the contrast determinations (see the text). The inset image is of the primary target showing no additional close-in companions.

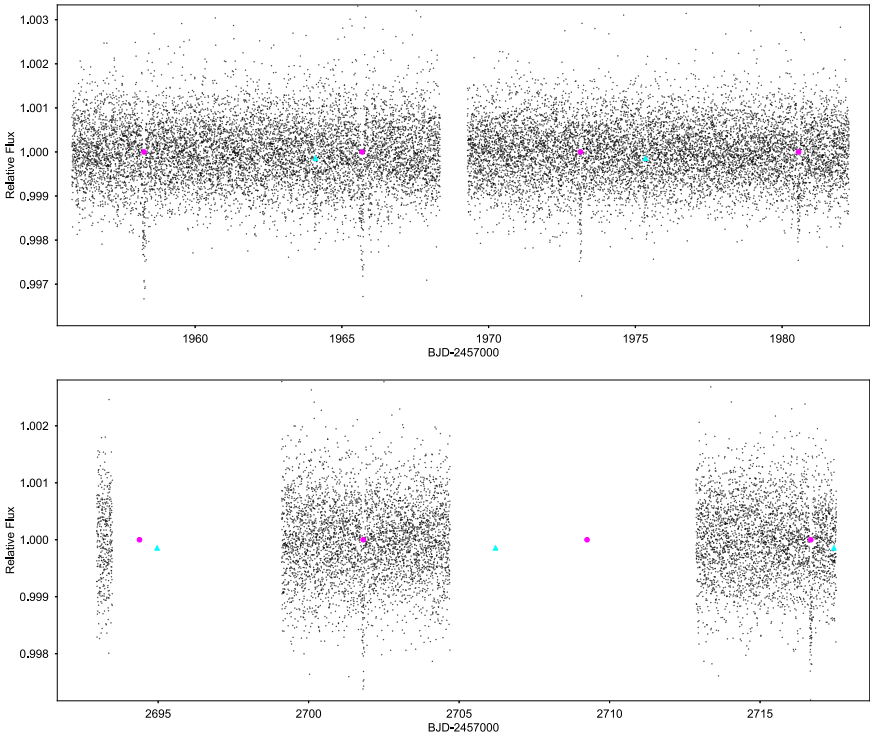

Figure 5. The detrended TESS light curve of TOI-2018. The color symbols indicate the transits of TOI-2018 b (magenta) and TOI-2018.02 (cyan).

excess noise, possibly caused by the presence of an unseen companion (e.g., Ziegler et al. 2020). TOI-2018 has a Gaia DR3 RUWE value of 1.23, indicating that the astrometric fits are consistent with the single-star model.

3. Photometric Analysis

3.1. TESS Observations

TOI-2018 (TIC 357501308) was observed by the TESS mission (Ricker et al. 2014) in Sectors 24 and 51. We started with the 2 minutes cadence light curve produced by the TESS Science Processing Operations Center (SPOC, located at the NASA Ames Research Center; Jenkins et al. 2016). The data were downloaded from the Mikulski Archive for Space Telescopes website[47] and are available at doi:10.17909/t9-nmc8-f686. Our subsequent analysis was based on the Presearch Data Conditioning Simple Aperture Photometry (Smith et al. 2012; Stumpe et al. 2012, 2014) version of the light curves, although the Simple Aperture Photometry (Twicken et al. 2010; Morris et al. 2020) version was used to measure the stellar rotation period, since it better preserves any long-term stellar variability. We excluded anomalous data points that have nonzero Quality flags. We note that the SPOC pipeline found a difference imaging centroid offset that is only $0\farcs945 \pm 2\farcs55$; this is again consistent with the lack of a nearby stellar companion for TOI-2018.

We removed any stellar activity or instrumental effects by fitting the light curve with a cubic spline in time of a width of 0.75 days. We searched for planetary transit signals in the detrended light curve using the Box Least Square algorithm (Kovács et al. 2002). Our pipeline was previously used for the detection of other K2 and TESS planets (Dai et al. 2017, 2021). We detected a 7.4 days planet with a signal detection efficiency (as defined by Kovács et al. 2002) of 11.7. The same candidate was reported by the TESS team (Guerrero et al. 2021) as TOI-2018.01. We also detected a second planet candidate at 11.3 days with a signal detection efficiency of 5.8, which is below the SPOC signal detection limit (S/N = 7.1). Given the low S/N of the detection, TOI-2018.02 does not meet the usual threshold for qualifying as a planet candidate. However, the orbital periods of the two planets are close to a 3:2 mean motion resonance with a small deviation of $(P_{\rm out}/P_{\rm in})/(3/2) - 1 \approx 1\%$, which may boost the case for a real planet for TOI-2018.02. We did not find any other significant transit signal in the TESS light curve. Figure 5 shows the detrended light curve and the transits of the two candidate planets.

We used the `Python` package `Batman` (Kreidberg 2015) to model the transit light curves of the two planets simultaneously. One of the global parameters is the mean stellar density of the host $\rho = 2.39 \pm 0.09 \rho_\odot$, as derived in Section 2. We imposed a Gaussian prior on the mean stellar density to help break the degeneracy in semimajor axis and impact parameter. Two other global parameters are the quadratic limb-darkening coefficients using the reparameterization of q_1 and q_2 suggested by Kipping (2013). We adopted a Gaussian prior using the theoretical values from `EXOFAST` (Eastman et al. 2013) and a standard deviation of 0.3. Both planets were assumed to have circular orbits, hence the other transit parameters are the orbital period $P_{\rm orb}$, the time of conjunction $T_{\rm c}$, the planet-to-star radius ratio $R_{\rm p}/R_\star$, the scaled orbital distance $a/R_\star$, and the transit impact parameter b.

We started by assuming that both planet candidates have linear ephemerides (i.e., no transit timing variations). We fitted all transits of each planet with a constant period model. The best-fit model was determined with the `Levenberg-Marquardt` method implemented in the `Python` package `lmfit` (Newville et al. 2014). This best-fit model was used as a

[47] https://archive.stsci.edu

Table 4
Model Parameters of TOI-2018

Parameter	Symbol	TOI-2018 b	TOI-2018.02
From Transit Modeling			
Mean Stellar Density ($\rho_\odot$)	$\rho_\star$	2.29 ± 0.22	-
Limb-darkening Coefficient	$q1$	0.36 ± 0.22	-
Limb-darkening Coefficient	$q2$	0.33 ± 0.23	-
Orbital Period (days)	$P_{\rm orb}$	7.435583 ± 0.000022	11.244 ± 0.025
Time of Conjunction (BJD-2457000)	t_c	1958.2580 ± 0.0013	1964.110 ± 0.020
Planet/Star Radius Ratio	$R_p/R_\star$	0.0335 ± 0.0010	0.0228 ± 0.0020
Impact Parameter	b	0.546 ± 0.070	0.16 ± 0.11
Scaled Semimajor Axis	$a/R_\star$	21.12 ± 0.69	27.82 ± 0.90
Transit Duration (hours)	T_{14}	2.360 ± 0.090	3.09 ± 0.12
Orbital Inclination (deg)	i	88.52 ± 0.22	89.66 ± 0.31
Orbital Eccentricity	e	0 (fixed)	0 (fixed)
From RV Modeling			
Semi-amplitude (m s^{-1})	K	4.4 ± 1.0	<1.5
GP Amplitude (m s^{-1})	h	5.0 ± 1.1	⋯
GP Correlation Timescale (days)	τ	$14.9^{+12.9}_{-9.4}$	⋯
GP Periodicity (days)	T	22.5 ± 2.1	⋯
GP Weighting	Γ	1.5 ± 0.3	⋯
RV Offset (m s^{-1})	γ	7.5 ± 3.8	⋯
RV Jitter (m s^{-1})	$\sigma_{\rm jit}$	$0.38^{+0.50}_{-0.24}$	⋯
RV Drift (m s^{-1} day^{-1})	$\dot{\gamma}$	-0.0017 ± 0.0008	⋯
Derived Parameters			
Planetary Radius ($R_\oplus$)	$R_{\rm p}$	2.268 ± 0.069	1.54 ± 0.14
Planetary Mass ($M_\oplus$)	$M_{\rm p}$	9.2 ± 2.1	<3.6

template transit to fit the mid-transit times of each individual transit. During the fits of individual transits, we varied only the mid-transit time and three parameters of a quadratic function of time that describes any residual long-term variations. A total of six and three transits were observed for the two planet candidates. We were not able to detect a statistically significant transit timing variation trend for either planet. We note that the transits of TOI-2018.02 in Sector 51 were either located in data gaps or near the end of the TESS observation (Figure 5). TOI-2018.02 could not be recovered using Sector 51 data alone. Our ephemeris of TOI-2018.02 is based on a joint fit using all sectors from TESS; the result has substantial uncertainty (Table 4), due to the ambiguity of the transit time in Sector 51. TESS will observe this system again in Sectors 77 and 78; those data will be instrumental in confirming TOI-2018.02 and for detecting transit timing variations. We carried out a Monte Carlo Markov Chain (MCMC) analysis using the `emcee` package (Foreman-Mackey et al. 2013). We initialized 128 walkers near the best-fit model from `lmfit`. We ran the MCMC for 50,000 links, which is more than two orders of magnitude longer than the typical autocorrelation function ($\lesssim$300 links). The resultant posterior distribution is summarized in Table 4. Figure 6 shows the phase-folded and binned light curves for each planet candidate as well as the best-fit transit model.

3.2. MuSCAT2 Observations

We observed two egresses of TOI-2018 b with the multiband imager MuSCAT2 (Narita et al. 2019) mounted on the 1.5 m Telescopio Carlos Sánchez at Teide Observatory, Spain. We obtained simultaneous g', r', i', and z_s photometry on the nights of 2022 June 15 and 2023 March 17. We performed basic data reduction (dark and flat correction), aperture photometry, and transit model fits including systematics with the MuSCAT2 pipeline (Parviainen et al. 2019). On both nights, we detected the egress of TOI-2018 b; the transit did not present any significant transit depth variations across the four MuSCAT2 bands. The transit times align well with those predicted from the TESS light curve, with no apparent transit timing variations. A joint fit of transit times from TESS and MuSCAT2 refined the transit ephemeris of TOI-2018 b: $P_{\rm orb} = 7.435569 \pm 0.000081$ days and T_c (BJD-2457000) $= 1958.25782 \pm 0.00058$. The MuSCAT2 data are also available on the ExoFOP website.

3.3. WASP Observations

TOI-2018 was observed by the WASP survey (Pollacco et al. 2006) from UT 2004 May 3 to 2007 June 28. The data are available at the following link.[48] We could not recover the transit signals of either TOI-2018 b or TOI-2018.02 in the WASP light curve (nondetection is expected, given the WASP light-curve quality). However, the much longer observational baseline of WASP provides a better constraint on the stellar rotation period than the TESS light curve.

4. RV Analysis

We acquired a total of 38 high-resolution spectra of TOI-2018 on Keck/HIRES (Vogt et al. 1994) from UT 2011 June 18 to 2021 August 30. These spectra were obtained with the iodine cell in the path of light. The iodine cell served as the reference for our wavelength solution and the line spread function. The exposure time is typically 300–600 s, after which we obtained a median S/N of 140 per reduced pixel near 5500

[48] https://exoplanetarchive.ipac.caltech.edu/docs/SuperWASPMission.html

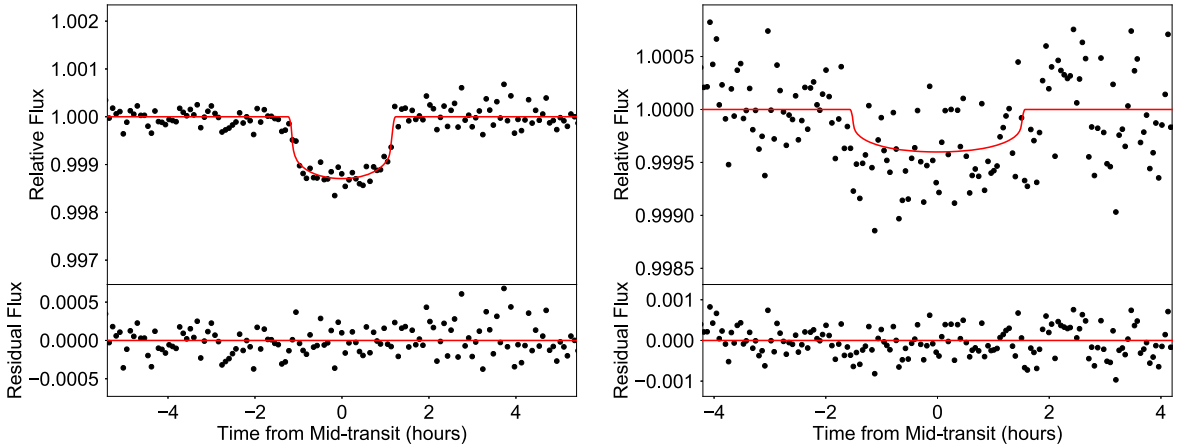

Figure 6. The phase-folded and binned transit light curves of TOI-2018 b (left) and TOI-2018.02 (right). The best-fit linear ephemeris model is shown in red. We note that TOI-2018.02 is below the typical S/N threshold (5.8 vs. 7.1) to be counted as a planet candidate.

Å. We extracted the RV using our forward-modeling Doppler code described in Howard et al. (2010). The estimated RV uncertainty is about 1.2 m s^{-1}. The extracted RVs and stellar activity indices are shown in Table 5.

We assumed that the planets are on circular orbits. We also experimented with nonzero eccentricities. However, the data at hand are not sufficiently constraining. The posterior samples prefer circular models with $\Delta\mathrm{BIC} > 10$. We simplified our analysis by focusing on circular orbits only. With circular orbits, the RV signals are hence described by the orbital period $P_{\rm orb}$, the time of inferior conjunction T_c, and the RV semi-amplitude K. We also included an RV offset γ, a linear RV trend $\dot{\gamma}$, and a jitter term σ_{jit} to account for any residual astrophysical or instrumental RV uncertainties. We imposed Gaussian priors on $P_{\rm orb}$ and T_c using the posterior distribution obtained from transit analysis. We imposed log-uniform priors on the RV semi-amplitude K and the jitter $\sigma_{\rm jit}$. We imposed uniform priors on the RV offset γ and linear trend $\dot{\gamma}$. To model the influence of stellar activity contamination in the RV data set, we employed a Gaussian Process (GP) model (e.g., Haywood et al. 2014; Grunblatt et al. 2015; Dai et al. 2017) with a quasiperiodic kernel:

$$C_{i,j} = h^2 \exp\left[-\frac{(t_i - t_j)^2}{2\tau^2} - \Gamma \sin^2 \frac{\pi (t_i - t_j)}{T}\right] + [\sigma_i^2 + \sigma_{\rm jit}^2]\delta_{i,j}, \quad (1)$$

where t_i is the time of individual RV measurements; $C_{i,j}$ is the covariance matrix; $\delta_{i,j}$ is the Kronecker delta function; h is the amplitude of the covariance; τ is the correlation timescale; Γ quantifies the relative significance between the squared exponential and periodic parts of the kernel; T is the period of the covariance; σ_i is the internal RV uncertainty; and σ_{jit} is the jitter term.

The corresponding likelihood function is

$$\log \mathcal{L} = -\frac{N}{2}\log 2\pi - \frac{1}{2}\log|\boldsymbol{C}| - \frac{1}{2}\boldsymbol{r}^{\rm T}\boldsymbol{C}^{-1}\boldsymbol{r}, \quad (2)$$

where N is the total number of RV measurements and $\boldsymbol{r}$ is the residual after subtracting the Keplerian planetary signals from the observed RV variation.

We first trained the GP model on the out-of-transit light curves. The underlying assumption is that the stellar surface magnetic activity drives both the out-of-transit flux variation in the light curve as well as a spurious quasi-sinusoidal contamination in RV measurement. Since the out-of-transit light curves are measured to higher precision and better sampled, we conditioned all the GP hyperparameters on the light curves first, before using those hyperparameters in the RV analysis.

We experimented with including increasingly more complexity to our RV models. We increased the number of planets included, and if a GP model for stellar activity was warranted by the RV data set, and if a linear RV trend $\dot{\gamma}$ was required, we selected the best model by examining the Bayesian Information Criterion (BIC) after model optimization with the `Levenberg-Marquardt` method `lmfit` (Newville et al. 2014). The model favored by the current data set contains only planet b, a long-term RV drift ($\dot{\gamma}$), and a GP model for the stellar activity. We sampled the posterior distribution of this model using a similar sampling procedure as described in Section 3, using EMCEE. We performed two separate samplings. The posterior distribution of the various hyperparameters from an MCMC analysis of the WASP light curve was used as a prior for a subsequent RV analysis. The underlying assumption is that the light curve is dominated by quasiperiodic flux variations due to the host's stellar activity. We summarize the posterior distribution of the RV analysis in Table 4. The RV variation of planet b is securely detected with more than 4σ significance (Figure 7). We note that the RV alone was able to independently discover planet b; the ephemeris of the planet from the transit analysis was crucial for recovering the RV signal. A linear RV drift $\dot{\gamma}$ is marginally detected at -0.0017 ± 0.0008 m s^{-1} day^{-1} over the 10 yr baseline of our HIRES observation. Unfortunately, the orbital period of TOI-2018.02 is close to the first harmonic of the rotation period (11.3 days versus 23.5/2 days; Figure 8). We were only able to place an upper limit on the mass of TOI-2018.02 ($<3.6 M_\oplus$ or $K < 1.5$ m s^{-1} at a 95% confidence level). Given the RV nondetection and the fact that only three transits were observed by TESS, we report TOI-2018.02 only as a possible planet candidate.

Table 5
Keck/HIRES RVs

Time (BJD)	RV (m s^{-1})	RV Unc. (m s^{-1})	S_{HK}	S_{HK} Unc.
2455730.958602	6.07	1.45	0.862	0.001
2455734.825559	8.22	1.28	0.924	0.001
2455738.787684	4.87	1.24	0.942	0.001
2459038.821696	13.18	1.17	0.980	0.001
2459040.797956	1.46	1.28	0.943	0.001
2459041.824545	−2.66	1.16	0.976	0.001
2459057.899283	1.45	1.48	0.923	0.001
2459379.877596	10.84	1.29	0.955	0.001
2459381.996691	−1.29	1.35	0.939	0.001
2459383.007785	−3.82	1.48	0.908	0.001
2459383.838423	−8.58	1.22	0.930	0.001
2459384.840558	−11.87	1.27	0.966	0.001
2459385.899575	−10.13	1.30	0.909	0.001
2459386.771843	−5.64	1.17	0.940	0.001
2459388.873567	−5.48	1.33	0.920	0.001
2459389.835862	−4.30	1.42	0.905	0.001
2459395.8831	1.87	1.23	0.895	0.001
2459397.962232	−0.29	1.49	0.873	0.001
2459399.786738	−2.54	1.24	0.902	0.001
2459404.959869	4.76	1.14	0.922	0.001
2459405.967385	−2.93	1.26	0.949	0.001
2459406.835315	−1.98	1.15	0.935	0.001
2459408.949042	1.34	1.18	0.907	0.001
2459409.954172	3.36	1.14	0.873	0.001
2459411.773495	−0.61	1.41	0.876	0.001
2459412.953324	−2.68	1.32	0.874	0.001
2459414.954138	1.18	1.44	0.888	0.001
2459422.908053	3.78	1.51	0.889	0.001
2459435.803746	−3.35	1.23	0.854	0.001
2459443.768482	−4.01	1.16	0.857	0.001
2459444.854338	−4.55	1.14	0.875	0.001
2459446.857033	13.66	1.54	0.928	0.001
2459448.79132	11.51	1.18	0.916	0.001
2459449.79849	6.07	1.23	0.925	0.001
2459451.81223	−3.59	1.11	0.960	0.001
2459452.74112	−1.93	1.11	0.945	0.001
2459455.773054	−3.80	1.26	0.886	0.001
2459456.806188	−3.19	1.27	0.890	0.001

5. Discussion

In Figure 9, we plot the measured masses and radii of the TOI-2018 planets and other confirmed exoplanets from the NASA Exoplanet Archive.[49] We also show various theoretical mass–radius relationships from Zeng et al. (2016), including 100%–Fe, 100%–$MgSiO_3$, and 100%–H_2O. In addition, we used the model by Chen & Rogers (2016) to generate the mass–radius relationships of planets with an Earthlike core and an H/He envelope of 0.5% and 1% in mass, taking into account the age and insolation of the planet as well. TOI-2018 b lies between 0.5% and 1% of H/He. However, TOI-2018 b is also consistent with an ice–rock mixture (H_2O–$MgSiO_3$). If we adopt a simple two-layer model (Zeng et al. 2016), TOI-2018 b is consistent with a 50%H_2O–50%$MgSiO_3$ composition, with a large uncertainty of about $50\% \pm 30\%$ in the water mass fraction. We also show the updated mass–radius curves for water worlds when supercritical water is included in the equation of state (Aguichine et al. 2021). TOI-2018 b is consistent with having a 20%-by-mass water/steam layer on top of an Earthlike core when the supercritical state is accounted for. With only mass and radius measurements, one cannot distinguish between an H/He-enveloped TOI-2018 b and a water-world TOI-2018 b. This ambiguity in composition is common to many exoplanets, which is why it has been difficult to resolve the ongoing debate over whether the observed bimodal radius distribution for sub-Neptune planets (Fulton et al. 2017) is due to the atmospheric erosion of H/He envelopes (e.g., Lopez & Fortney 2014; Owen & Wu 2017; Ginzburg et al. 2018) or the core growth model that gives rise to water worlds (e.g., Zeng et al. 2019; Luque & Pallé 2022; Piaulet et al. 2023). As noted by Luque & Pallé (2022), late-type stars may be well suited to settling this debate. Water worlds are expected to form beyond the snowline in the disk before migrating to the close-in orbits we see them in today. For late-type stars, the snowlines are generally much closer to the host star (Kennedy & Kenyon 2009). Moreover, Type I migration proceeds faster for planets with a higher planet-to-star mass ratio (see Kley & Nelson 2012, and references therein). The short migration scale and faster Type I migration rate both favor the migration of water worlds toward the late-type star. Disk migration might have deposited a sample of close-in water worlds (typically 50%H_2O–50%$MgSiO_3$) around late-type host stars, as reported by Luque & Pallé (2022). The composition of TOI-2018 b is consistent with a water-world interpretation. If future follow-up observations could confirm TOI-2018.02 and its near-resonant (1% wide of 3:2) configuration with TOI-2018 b, it would further support the hypothesis that the planets underwent inward migration. This is because Type I migration is a primary channel for capturing planets into mean motion resonances (e.g., Kley & Nelson 2012; Batygin 2015; Macdonald & Dawson 2018). Brewer et al. (2018) reported evidence that the fraction of compact, multiplanet systems is enhanced around low-metallicity host stars. If TOI-2018.02 can be confirmed by future observations, TOI-2018 presents another example of such an orbital architecture around a low-metallicity star.

With a mass of $9.2 \pm 2.1 M_\oplus$, TOI-2018 b is close to the threshold for runaway accretion and hence giant planet formation (Rafikov 2006; Lee & Chiang 2015; Lee 2019). Moreover, the low-metallicity (hence low-opacity) envelope of the planet should have cooled more easily and facilitated further accretion (Lee & Chiang 2015). Within the validity of these models, it might seem strange that TOI-2018 b failed to undergo runaway accretion, given the large core mass. Could this somehow be related to the suppressed occurrence rate of gas-giant planets around low-metallicity host stars (Fischer & Valenti 2005)? One possible explanation is that the disk lifetime is much shorter around lower-metallicity stars, as suggested by Yasui et al. (2010). Theoretically, the efficiency of the photoevaporation (and dissipation) of protoplanetary disks is enhanced at lower metallicity (the timescale for disk photoevaporation being $t_{\rm phot} \propto Z^{0.52}$; Ercolano & Clarke 2010). See also more recent hydrodynamic simulations by Nakatani et al. (2018). It may be the case that TOI-2018 b did not have enough time to initiate runaway accretion before the disk dissipated. Another relevant work by Wilson et al. (2022) has suggested that mini-Neptunes around low-metallicity host stars tend to have higher mean densities. It may indeed be the case that mini-Neptunes around low-metallicity stars typically do not accrete thick envelopes before the disks dissipate.

[49] https://exoplanetarchive.ipac.caltech.edu

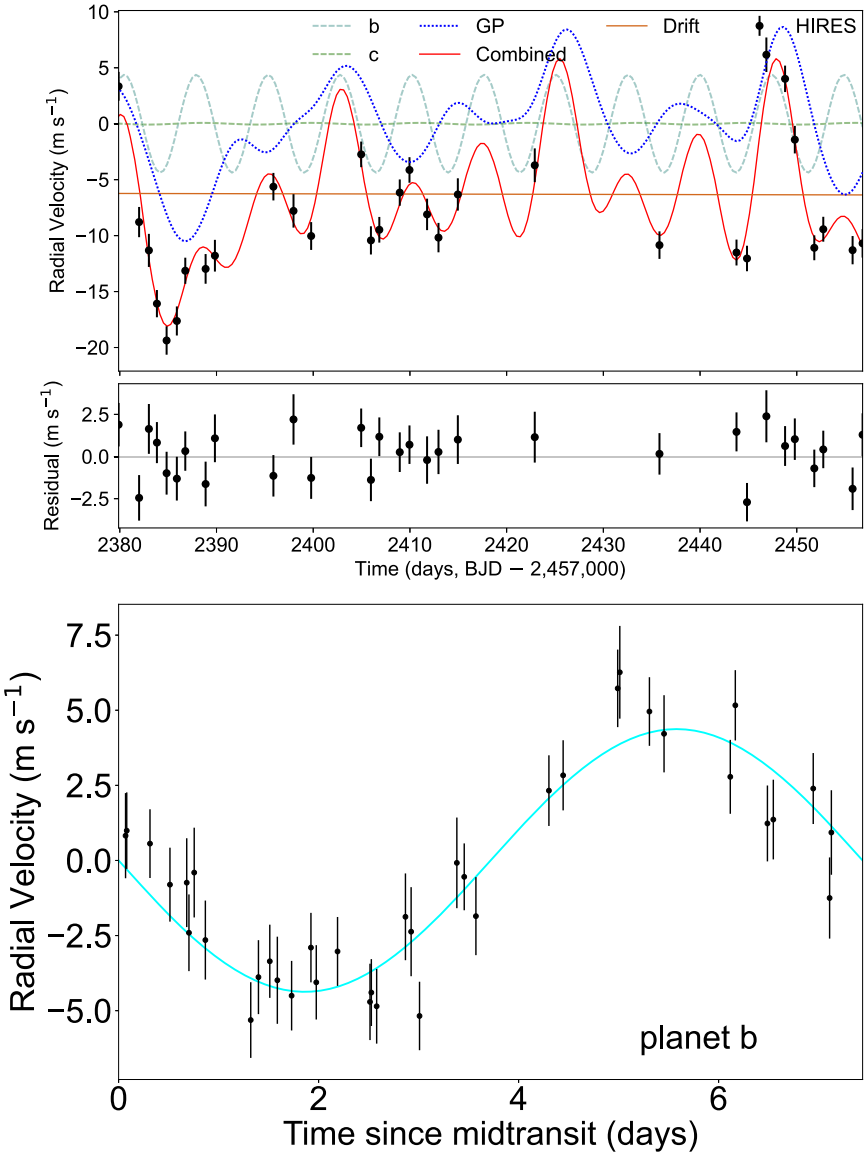

Figure 7. Top: the HIRES RV measurement of TOI-2018 (black symbols) and the best-fit RV model (red). The best-fit model only includes the contribution from TOI-2018 b (cyan), a RV drift (orange), and a GP model for stellar activity (blue). TOI-2018.02 (green dotted line) was not detected. Bottom: the RV measurements phase-folded at the orbital period of TOI-2018 b after removing the contribution from the other effects in the top panel.

One measurement that may distinguish a planet with an H/He envelope and a water world is to look for metastable Helium absorption due to the exosphere of the planet in the near-infrared (e.g., Oklopčić & Hirata 2018; Spake et al. 2018). K-type stars are ideal targets for metastable Helium observation, thanks to their balance of extreme UV to far-UV flux, which, respectively, excite and destroy the metastable He population (Oklopčić 2019; Wang & Dai 2021). A substantial metastable He population in turn leads to the absorption of the 10830 Å transition. With a *J*-band magnitude of 7.8 and a moderately active K-type host, TOI-2018 b is a favorable target for looking for metastable Helium absorption. The detection of ongoing Helium escape would strongly favor an H/He envelope that has survived photoevaporation.

We quantify the observability of TOI-2018 b in transmission spectroscopy using the James Webb Space Telescope (JWST; Gardner et al. 2006). We computed the Transmission Spectroscopy Metric (TSM), as suggested by Kempton et al. (2018). TOI-2018 b has a TSM of roughly 103. Although there are dozens of known exoplanets that have higher TSMs (Figure 10), TOI-2018 b does provide a rare opportunity to probe the atmospheric composition of planets formed in a low-metallicity environment. It is one of the top-ranking TSM targets, with [Fe/H] < -0.5. Given how bright the host is ($J = 7.8$, $K = 7.1$), special attention to the choice of instruments and observation modes is required to avoid saturation.

Previous results by Brinkman et al. (2023) and Demangeon et al. (2021) may suggest that super-Earths formed around low-metallicity late-type stars (L 98-59 M dwarf, [Fe/H] $= -0.46 \pm 0.26$ and TOI-561 K dwarf, [Fe/H] $= -0.41 \pm 0.05$) have lower mean densities than super-Earths around Sunlike stars. A similar trend was also pointed out by Adibekyan et al. (2021) and Castro-González et al. (2023). The lower mean densities may be the result of an alternative planet formation pathway in the low-metallicity regime. The enhanced α-element abundance (Mg, Ca, and Si) compared to Fe naturally favors the formation of a larger mantle than an

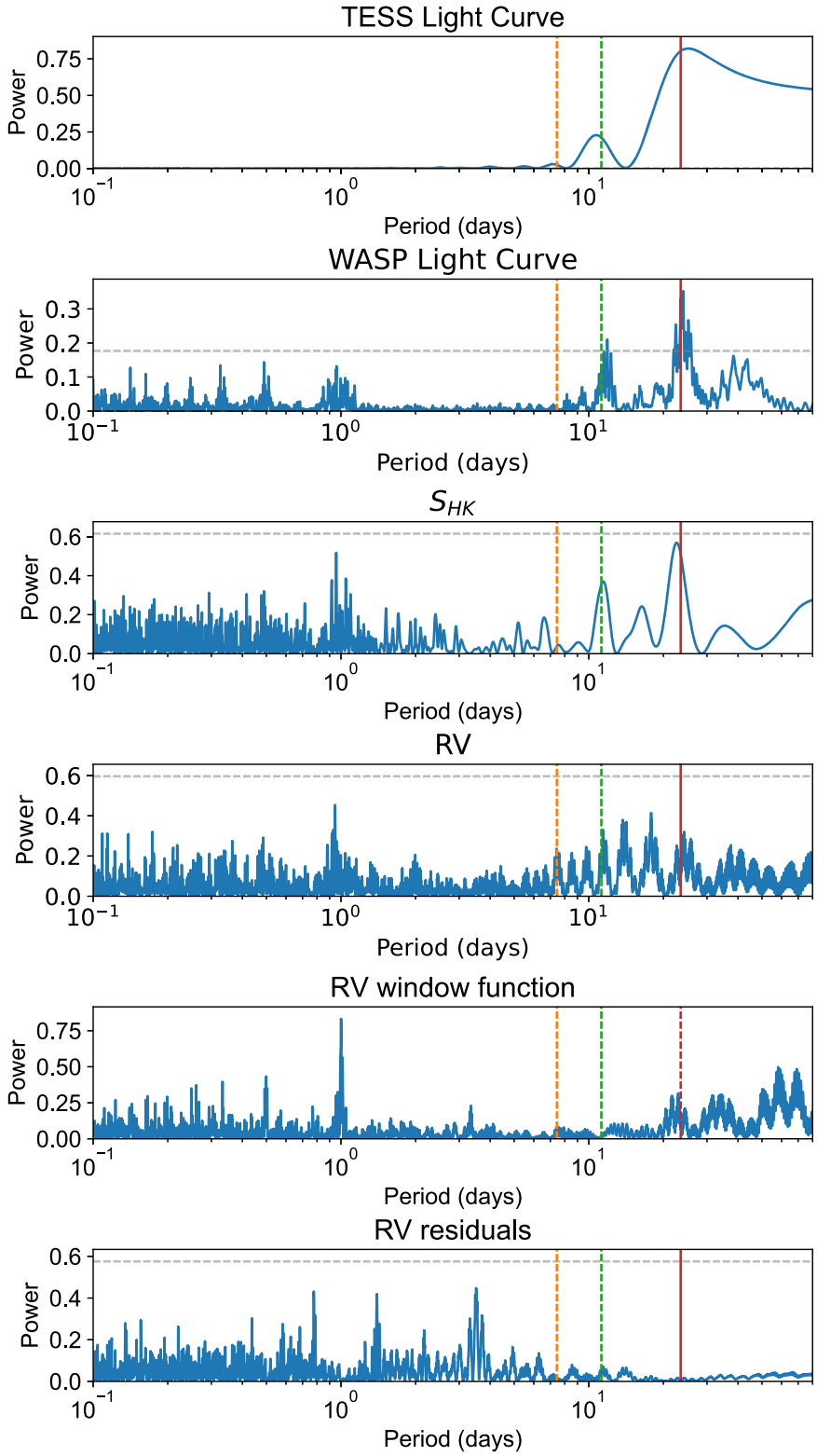

Figure 8. The Lomb–Scargle periodograms of the TESS light curve, the WASP light curve, the HIRES S_{HK} activity indicator, the measured RVs, the RV window function, and the RV residuals after subtracting the best-fit model (Figure 7). The vertical lines are, respectively, the orbital periods of TOI-2018 b (orange dashed line) and TOI-2018.02 (green dashed line), and the rotation period of the host star (red solid line). Whenever appropriate, we included horizontal dashed lines to indicate the 1% false alarm levels.

iron/nickel core. If so, one might expect planets around low-metallicity stars (particularly thick-disk stars) to have lower mean densities compared to solar-type stars. The literature contains only a handful of mass and radius measurements for planets around low-metallicity host stars ([Fe/H] < -0.4). More metal-poor systems and more precise characterizations of these planets are needed to evaluate their composition as a population.

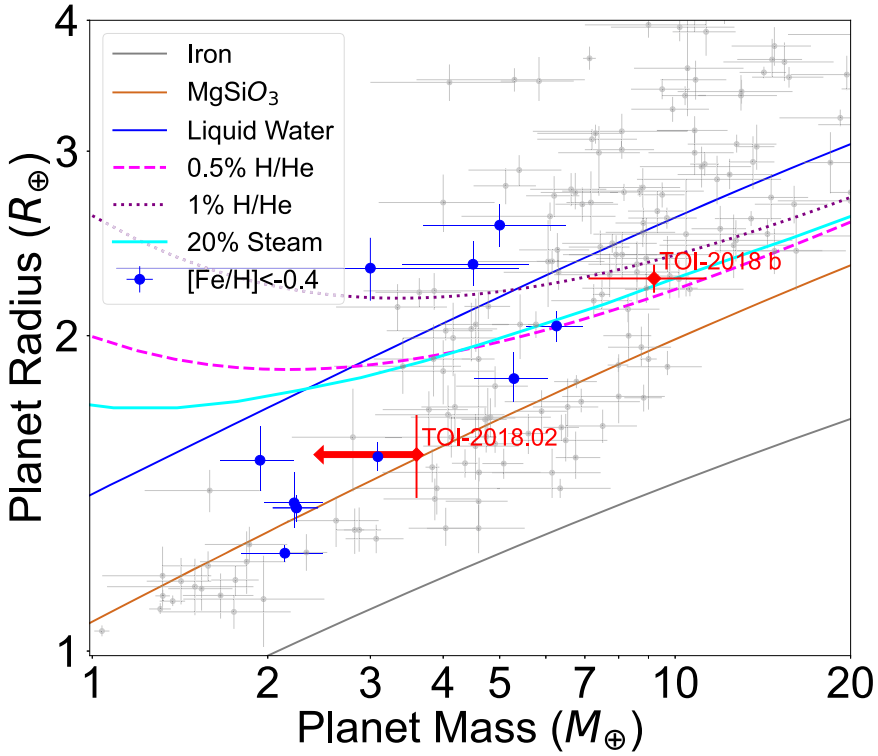

Figure 9. The mass and radius measurements of TOI-2018 b and TOI-2018.02 (upper limits only). The solid curves are theoretical mass–radius curves from Zeng et al. (2016). The dotted and dashed lines are mass–radius curves for planets with an Earthlike core and an H/He envelope of varying mass ratios (Chen & Rogers 2016). We also show the updated mass–radius curves for water worlds when the supercritical state of water is taken into account in the equation of state (the cyan curve shows a 20%-by-mass water layer on top of an Earthlike core; Aguichine et al. 2021). We highlight other planets around low-metallicity host stars (blue symbols; [Fe/H] < -0.4). Even super-Earth ($<1.5R_\oplus$; Rogers 2015) planets around low-metallicity stars seem to favor a lower mean density.

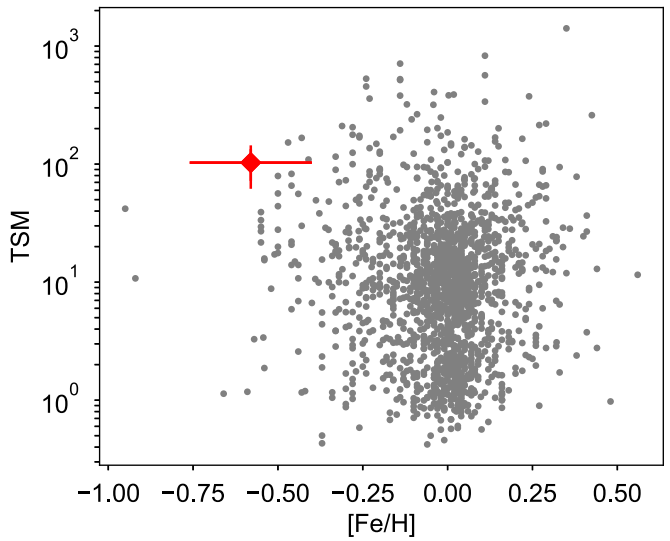

Figure 10. The host metallicity [Fe/H] vs. the TSM (Kempton et al. 2018) of TOI-2018 b (red) and confirmed exoplanets with a mini-Neptune size ($<3R_\oplus$). TOI-2018 b has an estimated TSM of 103.

We thank Heather Knutson, Yayaati Chachan, Kento Masuda, and Yanqin Wu for helpful discussion.

This material is based on work supported by the TESS General Investigator program under NASA grant 80NSSC20K0059.

D.H. acknowledges support from the Alfred P. Sloan Foundation, the National Aeronautics and Space Administration (80NSSC21K0652), and the Australian Research Council (FT200100871).

J.M.A.M. is supported by the National Science Foundation (NSF) Graduate Research Fellowship Program under grant No. DGE-1842400. J.M.A.M. acknowledges the LSSTC Data Science Fellowship Program, which is funded by LSSTC, NSF Cybertraining grant No. 1829740, the Brinson Foundation, and the Moore Foundation; his participation in the program has benefited this work.

This article is based on observations made with the MuSCAT2 instrument, developed by ABC, at Telescopio Carlos Sánchez, operated on the island of Tenerife by the IAC in the Spanish Observatorio del Teide. This work is partly financed by the Spanish Ministry of Economics and Competitiveness through grants PGC2018-098153-B-C31.

This work is partly supported by JSPS KAKENHI grant No. JP18H05439 and JST CREST grant No. JPMJCR1761. This article is based on observations made with the MuSCAT2 instrument, developed by ABC, at Telescopio Carlos Sánchez, operated on the island of Tenerife by the IAC in the Spanish Observatorio del Teide.

D.R.C. acknowledges partial support from NASA grant 18-2XRP18_2-0007.

A.A.B. acknowledges the support of the Ministry of Science and Higher Education of the Russian Federation under the grant 075-15-2020-780 (N13.1902.21.0039).

The data presented herein were obtained at the W. M. Keck Observatory, which is operated as a scientific partnership among the California Institute of Technology, the University of California, and the National Aeronautics and Space

Administration. The Observatory was made possible by the generous financial support of the W. M. Keck Foundation.

The authors wish to recognize and acknowledge the very significant cultural role and reverence that the summit of Maunakea has always had within the indigenous Hawaiian community. We are most fortunate to have the opportunity to conduct observations from this mountain.

We acknowledge the use of public TESS data from pipelines at the TESS Science Office and at the TESS Science Processing Operations Center. Resources supporting this work were provided by the NASA High-End Computing (HEC) Program through the NASA Advanced Supercomputing (NAS) Division at Ames Research Center for the production of the SPOC data products.

J.L.-B. acknowledges financial support from the Spanish Ministerio de Ciencia e Innovaci (MCIN/AEI/ 10.13039/501100011033) and the European Union NextGeneration EU/PRTR under the Ramon y Cajal program with code RYC2021-031640-I. Based on observations collected at the Centro Astronomico Hispano en Andalucia (CAHA) at Calar Alto, operated jointly by Junta de Andalucia and Consejo Superior de Investigaciones Cientificas (IAA-CSIC).

A.C.-G. is funded by the Spanish Ministry of Science through MCIN/AEI/10.13039/501100011033 grant PID2019-107061GB-C61.

This paper has made use of data collected by the TESS mission that are publicly available from the Mikulski Archive for Space Telescopes (MAST), operated by the Space Telescope Science Institute (STScI).

Funding for the TESS mission is provided by NASA's Science Mission Directorate.

Some of the observations in this paper made use of the High-Resolution Imaging instrument Alopeke and were obtained under Gemini LLP Proposal Number GN/S-2021A-LP-105. Alopeke was funded by the NASA Exoplanet Exploration Program and built at the NASA Ames Research Center by Steve B. Howell, Nic Scott, Elliott P. Horch, and Emmett Quigley. Alopeke was mounted on the Gemini North telescope of the international Gemini Observatory, a program of NSF's NOIR Lab, which is managed by the Association of Universities for Research in Astronomy (AURA) under a cooperative agreement with the National Science Foundation on behalf of the Gemini partnership: the National Science Foundation (United States), National Research Council (Canada), Agencia Nacional de Investigación y Desarrollo (Chile), Ministerio de Ciencia, Tecnología e Innovación (Argentina), Ministério da Ciência, Tecnologia, Inovações e Comunicações (Brazil), and the Korea Astronomy and Space Science Institute (Republic of Korea).

Facilities: Keck: I (HIRES), TESS, MuSCAT2, WASP, Palomar, Lick, Gemini, Carlo ALto, Caucasian Observatory of Sternberg Astronomical Institute.

Software: ASTROIMAGE (Collins et al. 2017), ISOCLASSIFY (Huber et al. 2017), ISOCHRONES (Morton 2015), MIST (Choi et al. 2016), SPECMATCH-SYN (Petigura 2015), BATMAN (Kreidberg 2015), EMCEE (Foreman-Mackey et al. 2013), ISPEC (Blanco-Cuaresma et al. 2014; Blanco-Cuaresma 2019), COLTE (Casagrande et al. 2021).

ORCID iDs

Fei Dai https://orcid.org/0000-0002-8958-0683
Kevin C. Schlaufman https://orcid.org/0000-0001-5761-6779
Henrique Reggiani https://orcid.org/0000-0001-6533-6179
Luke Bouma https://orcid.org/0000-0002-0514-5538
Andrew W. Howard https://orcid.org/0000-0001-8638-0320
Ashley Chontos https://orcid.org/0000-0003-1125-2564
Daria Pidhorodetska https://orcid.org/0000-0001-9771-7953
Judah Van Zandt https://orcid.org/0000-0002-4290-6826
Joseph M. Akana Murphy https://orcid.org/0000-0001-8898-8284
Ryan A. Rubenzahl https://orcid.org/0000-0003-3856-3143
Alex S. Polanski https://orcid.org/0000-0001-7047-8681
Jack Lubin https://orcid.org/0000-0001-8342-7736
Corey Beard https://orcid.org/0000-0001-7708-2364
Steven Giacalone https://orcid.org/0000-0002-8965-3969
Rae Holcomb https://orcid.org/0000-0002-5034-9476
Natalie M. Batalha https://orcid.org/0000-0002-7030-9519
Courtney Dressing https://orcid.org/0000-0001-8189-0233
Benjamin Fulton https://orcid.org/0000-0003-3504-5316
Daniel Huber https://orcid.org/0000-0001-8832-4488
Howard Isaacson https://orcid.org/0000-0002-0531-1073
Stephen R. Kane https://orcid.org/0000-0002-7084-0529
Erik A. Petigura https://orcid.org/0000-0003-0967-2893
Paul Robertson https://orcid.org/0000-0003-0149-9678
Lauren M. Weiss https://orcid.org/0000-0002-3725-3058
Alexander A. Belinski https://orcid.org/0000-0003-2228-7914
Andrew W. Boyle https://orcid.org/0000-0001-6037-2971
Christopher J. Burke https://orcid.org/0000-0002-7754-9486
Amadeo Castro-González https://orcid.org/0000-0001-7439-3618
David R. Ciardi https://orcid.org/0000-0002-5741-3047
Tansu Daylan https://orcid.org/0000-0002-6939-9211
Akihiko Fukui https://orcid.org/0000-0002-4909-5763
Holden Gill https://orcid.org/0000-0001-6171-7951
Natalia M. Guerrero https://orcid.org/0000-0002-5169-9427
Coel Hellier https://orcid.org/0000-0002-3439-1439
Steve B. Howell https://orcid.org/0000-0002-2532-2853
Jorge Lillo-Box https://orcid.org/0000-0003-3742-1987
Felipe Murgas https://orcid.org/0000-0001-9087-1245
Norio Narita https://orcid.org/0000-0001-8511-2981
Enric Pallé https://orcid.org/0000-0003-0987-1593
Arjun B. Savel https://orcid.org/0000-0002-2454-768X
Avi Shporer https://orcid.org/0000-0002-1836-3120
Keivan G. Stassun https://orcid.org/0000-0002-3481-9052
Stephanie Striegel https://orcid.org/0009-0008-5145-0446
Jon M. Jenkins https://orcid.org/0000-0002-4715-9460
George R. Ricker https://orcid.org/0000-0003-2058-6662
Sara Seager https://orcid.org/0000-0002-6892-6948
Roland Vanderspek https://orcid.org/0000-0001-6763-6562
Joshua N. Winn https://orcid.org/0000-0002-4265-047X

References

Adibekyan, V., Dorn, C., Sousa, S. G., et al. 2021, Sci, 374, 330
Aguichine, A., Mousis, O., Deleuil, M., & Marcq, E. 2021, ApJ, 914, 84
Albareti, F. D., Allende Prieto, C., Almeida, A., et al. 2017, ApJS, 233, 25
Arenou, F., Luri, X., Babusiaux, C., et al. 2018, A&A, 616, A17
Asplund, M., Amarsi, A. M., & Grevesse, N. 2021, A&A, 653, A141
Batygin, K. 2015, MNRAS, 451, 2589
Bensby, T., Feltzing, S., & Oey, M. S. 2014, A&A, 562, A71
Blanco-Cuaresma, S. 2019, MNRAS, 486, 2075
Blanco-Cuaresma, S., Soubiran, C., Heiter, U., & Jofré, P. 2014, A&A, 569, A111

Borucki, W. J., Koch, D. G., Basri, G., et al. 2011, ApJ, 728, 117
Bouma, L. G., Kerr, R., Curtis, J. L., et al. 2022, AJ, 164, 215
Bouma, L. G., Palumbo, E. K., & Hillenbrand, L. A. 2023, ApJL, 947, L3
Brewer, J. M., Wang, S., Fischer, D. A., & Foreman-Mackey, D. 2018, ApJL, 867, L3
Brinkman, C., Weiss, L. M., Dai, F., et al. 2023, AJ, 165, 88
Buder, S., Sharma, S., Kos, J., et al. 2021, MNRAS, 506, 150
Capitanio, L., Lallement, R., Vergely, J. L., Elyajouri, M., & Monreal-Ibero, A. 2017, A&A, 606, A65
Carrillo, A., Hawkins, K., Bowler, B. P., Cochran, W., & Vanderburg, A. 2020, MNRAS, 491, 4365
Casagrande, L., Lin, J., Rains, A. D., et al. 2021, MNRAS, 507, 2684
Castro-González, A., Demangeon, O. D. S., Lillo-Box, J., et al. 2023, arXiv:2305.04922
Chen, H., & Rogers, L. A. 2016, ApJ, 831, 180
Choi, J., Dotter, A., Conroy, C., et al. 2016, ApJ, 823, 102
Ciardi, D. R., Beichman, C. A., Horch, E. P., & Howell, S. B. 2015, ApJ, 805, 16
Collins, K. A., Kielkopf, J. F., Stassun, K. G., & Hessman, F. V. 2017, AJ, 153, 77
Cui, X.-Q., Zhao, Y.-H., Chu, Y.-Q., et al. 2012, RAA, 12, 1197
Dai, F., Howard, A. W., Batalha, N. M., et al. 2021, AJ, 162, 62
Dai, F., Winn, J. N., Gandolfi, D., et al. 2017, AJ, 154, 226
Dekany, R., Roberts, J., Burruss, R., et al. 2013, ApJ, 776, 130
Demangeon, O. D. S., Zapatero Osorio, M. R., Alibert, Y., et al. 2021, A&A, 653, A41
Eastman, J., Gaudi, B. S., & Agol, E. 2013, PASP, 125, 83
Ercolano, B., & Clarke, C. J. 2010, MNRAS, 402, 2735
Evans, D. W., Riello, M., De Angeli, F., et al. 2018, A&A, 616, A4
Fabricius, C., Luri, X., Arenou, F., et al. 2021, A&A, 649, A5
Feroz, F., Hobson, M. P., & Bridges, M. 2009, MNRAS, 398, 1601
Feroz, F., Hobson, M. P., Cameron, E., & Pettitt, A. N. 2013, arXiv:1306.2144
Fischer, D. A., & Valenti, J. 2005, ApJ, 622, 1102
Foreman-Mackey, D., Hogg, D. W., Lang, D., & Goodman, J. 2013, PASP, 125, 306
Fressin, F., Torres, G., Charbonneau, D., et al. 2013, ApJ, 766, 81
Fulton, B. J., Petigura, E. A., Howard, A. W., et al. 2017, AJ, 154, 109
Furlan, E., Ciardi, D. R., Everett, M. E., et al. 2017, AJ, 153, 71
Gagné, J., Mamajek, E. E., Malo, L., et al. 2018, ApJ, 856, 23
Gaia Collaboration, Brown, A. G. A., Vallenari, A., et al. 2018, A&A, 616, A1
Gaia Collaboration, Prusti, T., de Bruijne, J. H. J., et al. 2016, A&A, 595, A1
Gaia Collaboration, Vallenari, A., Brown, A. G. A., et al. 2023, A&A, 674, A1
Gardner, J. P., Mather, J. C., Clampin, M., et al. 2006, SSRv, 123, 485
Gavel, D., Kupke, R., Dillon, D., et al. 2014, Proc SPIE, 9148, 914805
Ginzburg, S., Schlichting, H. E., & Sari, R. 2018, MNRAS, 476, 759
Gonzalez, G. 1997, MNRAS, 285, 403
Grunblatt, S. K., Howard, A. W., & Haywood, R. D. 2015, ApJ, 808, 127
Guerrero, N. M., Seager, S., Huang, C. X., et al. 2021, ApJS, 254, 39
Gustafsson, B., Edvardsson, B., Eriksson, K., et al. 2008, A&A, 486, 951
Hambly, N. C., Cropper, M., Boudreault, S., et al. 2018, A&A, 616, A15
Hayashi, C. 1981, PThPS, 70, 35
Hayward, T. L., Brandl, B., Pirger, B., et al. 2001, PASP, 113, 105
Haywood, R. D., Collier Cameron, A., Queloz, D., et al. 2014, MNRAS, 443, 2517
Hormuth, F., Brandner, W., Hippler, S., & Henning, T. 2008, JPhCS, 131, 012051
Howard, A. W., Johnson, J. A., Marcy, G. W., et al. 2010, ApJ, 721, 1467
Howard, A. W., Marcy, G. W., Bryson, S. T., et al. 2012, ApJS, 201, 15
Howell, S. B., Everett, M. E., Sherry, W., Horch, E., & Ciardi, D. R. 2011, AJ, 142, 19
Huber, D., Zinn, J., Bojsen-Hansen, M., et al. 2017, ApJ, 844, 102
Isaacson, H., & Fischer, D. 2010, ApJ, 725, 875
Jenkins, J. M., Twicken, J. D., McCauliff, S., et al. 2016, Proc. SPIE, 9913, 99133E
Kempton, E. M. R., Bean, J. L., Louie, D. R., et al. 2018, PASP, 130, 114401
Kennedy, G. M., & Kenyon, S. J. 2009, ApJ, 695, 1210
Kipping, D. M. 2013, MNRAS, 435, 2152
Kley, W., & Nelson, R. P. 2012, ARA&A, 50, 211
Kovács, G., Zucker, S., & Mazeh, T. 2002, A&A, 391, 369
Kreidberg, L. 2015, PASP, 127, 1161
Kupke, R., Gavel, D., Roskosi, C., et al. 2012, Proc. SPIE, 8447, 84473G
Kurucz, R. L. 1979, ApJS, 40, 1
Lallement, R., Capitanio, L., Ruiz-Dern, L., et al. 2018, A&A, 616, A132
Lallement, R., Vergely, J. L., Valette, B., et al. 2014, A&A, 561, A91
Lee, E. J. 2019, ApJ, 878, 36
Lee, E. J., & Chiang, E. 2015, ApJ, 811, 41
Lee, E. J., & Chiang, E. 2016, ApJ, 817, 90
Lee, E. J., Chiang, E., & Ferguson, J. W. 2018, MNRAS, 476, 2199
Lindegren, L., Bastian, U., Biermann, M., et al. 2021a, A&A, 649, A4
Lindegren, L., Klioner, S. A., Hernández, J., et al. 2021b, A&A, 649, A2
Lomb, N. R. 1976, Ap&SS, 39, 447
Lopez, E. D., & Fortney, J. J. 2014, ApJ, 792, 1
Lund, M. B., & Ciardi, D. 2020, AAS Meeting Abstracts, 235, 249.06
Luque, R., & Pallé, E. 2022, Sci, 377, 1211
Macdonald, M. G., & Dawson, R. I. 2018, AJ, 156, 228
Mamajek, E. E., & Hillenbrand, L. A. 2008, ApJ, 687, 1264
Martig, M., Rix, H.-W., Silva Aguirre, V., et al. 2015, MNRAS, 451, 2230
McGurk, R., Rockosi, C., Gavel, D., et al. 2014, Proc. SPIE, 9148, 91483A
McQuillan, A., Mazeh, T., & Aigrain, S. 2014, ApJS, 211, 24
Meléndez, J., Schirbel, L., Monroe, T. R., et al. 2014, A&A, 567, L3
Morris, R. L., Twicken, J. D., Smith, J. C., et al. 2020, Kepler Science Document KSCI-19081-003
Morton, T. D. 2015 isochrones: Stellar model grid package, Astrophysics Source Code Library, ascl:1503.010
Mugrauer, M., & Michel, K.-U. 2020, AN, 341, 996
Mugrauer, M., & Michel, K.-U. 2021, AN, 342, 840
Mugrauer, M., Zander, J., & Michel, K.-U. 2022, AN, 343, e24017
Nakatani, R., Hosokawa, T., Yoshida, N., Nomura, H., & Kuiper, R. 2018, ApJ, 857, 57
Narita, N., Fukui, A., Kusakabe, N., et al. 2019, JATIS, 5, 015001
Newville, M., Stensitzki, T., Allen, D. B., & Ingargiola, A. 2014, LMFIT: Nonlinear Least-Square Minimization and Curve-Fitting for Python, v0.8.0, Zenodo, doi:10.5281/zenodo.11813
Oklopčić, A. 2019, ApJ, 881, 133
Oklopčić, A., & Hirata, C. M. 2018, ApJL, 855, L11
Owen, J. E., & Wu, Y. 2017, ApJ, 847, 29
Parviainen, H., Tingley, B., Deeg, H. J., et al. 2019, A&A, 630, A89
Paxton, B., Bildsten, L., Dotter, A., et al. 2011, ApJS, 192, 3
Paxton, B., Cantiello, M., Arras, P., et al. 2013, ApJS, 208, 4
Paxton, B., Marchant, P., Schwab, J., et al. 2015, ApJS, 220, 15
Petigura, E. A. 2015, PhD thesis, Univ. California, Berkeley
Petigura, E. A., Howard, A. W., & Marcy, G. W. 2013, PNAS, 110, 19273
Petigura, E. A., Marcy, G. W., Winn, J. N., et al. 2018, AJ, 155, 89
Piaulet, C., Benneke, B., Almenara, J. M., et al. 2023, NatAs, 7, 206
Pollacco, D. L., Skillen, I., Collier Cameron, A., et al. 2006, PASP, 118, 1407
Pollack, J. B., Hubickyj, O., Bodenheimer, P., et al. 1996, Icar, 124, 62
Rafikov, R. R. 2006, ApJ, 648, 666
Reggiani, H., Schlaufman, K. C., Healy, B. F., Lothringer, J. D., & Sing, D. K. 2022, AJ, 163, 159
Ricker, G. R., Winn, J. N., Vanderspek, R., et al. 2014, Proc. SPIE, 9143, 914320
Riello, M., De Angeli, F., Evans, D. W., et al. 2018, A&A, 616, A3
Rogers, L. A. 2015, ApJ, 801, 41
Safonov, B. S., Lysenko, P. A., & Dodin, A. V. 2017, AstL, 43, 344
Santos, N. C., Israelian, G., & Mayor, M. 2004, A&A, 415, 1153
Scargle, J. D. 1982, ApJ, 263, 835
Smith, J. C., Stumpe, M. C., Van Cleve, J. E., et al. 2012, PASP, 124, 1000
Sneden, C. 1973, ApJ, 184, 839
Sneden, C., Bean, J., Ivans, I., Lucatello, S., & Sobeck, J. 2012 MOOG: LTE line analysis and spectrum synthesis, Astrophysics Source Code Library, ascl:1202.009
Spake, J. J., Sing, D. K., Evans, T. M., et al. 2018, Natur, 557, 68
Stassun, K. G., Oelkers, R. J., Paegert, M., et al. 2019, AJ, 158, 138
Stassun, K. G., & Torres, G. 2016, AJ, 152, 180
Steinmetz, M., Matijevič, G., Enke, H., et al. 2020, AJ, 160, 82
Stumpe, M. C., Smith, J. C., Catanzarite, J. H., et al. 2014, PASP, 126, 100
Stumpe, M. C., Smith, J. C., Van Cleve, J. E., et al. 2012, PASP, 124, 985
Tayar, J., Claytor, Z. R., Huber, D., & van Saders, J. 2022, ApJ, 927, 31
Torra, F., Castañeda, J., Fabricius, C., et al. 2021, A&A, 649, A10
Twicken, J. D., Clarke, B. D., Bryson, S. T., et al. 2010, Proc. SPIE, 7740, 774023
Vogt, S. S., Allen, S. L., Bigelow, B. C., et al. 1994, Proc. SPIE, 2198, 362
Wang, J., & Fischer, D. A. 2015, AJ, 149, 14
Wang, L., & Dai, F. 2021, ApJ, 914, 98
Wilson, T. G., Goffo, E., Alibert, Y., et al. 2022, MNRAS, 511, 1043
Yana Galarza, J., Meléndez, J., Lorenzo-Oliveira, D., et al. 2019, MNRAS, 490, L86
Yasui, C., Kobayashi, N., Tokunaga, A. T., Saito, M., & Tokoku, C. 2010, ApJL, 723, L113
Zeng, L., Jacobsen, S. B., Sasselov, D. D., et al. 2019, PNAS, 116, 9723
Zeng, L., Sasselov, D. D., & Jacobsen, S. B. 2016, ApJ, 819, 127
Ziegler, C., Tokovinin, A., Briceño, C., et al. 2020, AJ, 159, 19